nature communications

Article

https://doi.org/10.1038/s41467-025-64493-w

Giant shot noise in superconductor/ferromagnet junctions with orbital-symmetry- controlled spin-orbit coupling

Received: 25 March 2025

Accepted: 18 September 2025

Published online: 28 October 2025

Check for updates

César González-Ruano[1,2,9], Chenghao Shen[3,4,9], Pablo Tuero[1,9], Coriolan Tiusan[5], Yuan Lu[6], Jong E. Han[3], Igor Žutić[3] ✉ & Farkhad G. Aliev[1,7,8] ✉

By measuring the shot noise, a consequence of charge quantization, in superconductor/insulator/ferromagnet (V/MgO/Fe) junctions, we discover a giant increase, orders of magnitude larger than expected. The origin of this giant noise is a peculiar realization of a superconducting proximity effect, where a simple superconductor influences its neighbors. Our measurements reveal largely unexplored implications of orbital-symmetry-controlled proximity effects. The importance of orbital symmetries and the accompanying spin-orbit coupling is manifested by an unexpected emergence of another superconducting region, strikingly different from the parent superconductor. Unlike vanadium's common spin-singlet superconductivity, the broken inversion symmetry in V/MgO/Fe junctions and the resulting interfacial spin-orbit coupling lead to the formation of spin-triplet superconductivity across the ferromagnetic iron. Here, we show that the enhanced shot noise, known from Josephson junctions with two superconductors, is measured even in a single superconductor. This discovery motivates revisiting how the spin-orbit coupling and superconducting proximity effects can transform many materials.

A common goal in science and technology is to suppress noise and increase the signal-to-noise ratio[1–3]. However, noise also enables elucidating subtle phenomena, hidden from other experimental probes[4–9]. A striking example is shot noise, which can be used to characterize strongly-correlated systems, strange metals, quantum entanglement, or fractionally charged quasiparticles[7–11]. Since shot noise stems from charge quantization, the fractional quantum Hall effect can be characterized by the reduced shot noise, while in superconductors, where the charge is added in Cooper pairs, even doubling of the normal-state shot noise is possible. The concept of proximity effects, where a given material is influenced by its neighbors, has been known for superconductors for over ninety years[12,13]. In Josephson junctions, where the superconductivity from the *two superconductors* can leak across the nonsuperconducting region, the proximity effects have been identified through the observation of multiple reflections of Cooper pairs and accompanied by a large, measured shot noise[14–16]. While proximity effects have been extensively studied in junctions with a *single* superconducting region, so far,

[1]Departamento Física de la Materia Condensada C-III, Universidad Autónoma de Madrid, Madrid, Spain. [2]Institute for Research and Technology (IIT), School of Engineering (ICAI), Universidad Pontificia Comillas, Madrid, Spain. [3]Department of Physics, University at Buffalo, State University of New York, Buffalo, NY, USA. [4]Eastern Institute for Advanced Study, Eastern Institute of Technology, Ningbo, Zhejiang, China. [5]Department of Solid State Physics and Advanced Technologies, Faculty of Physics, Babes- Bolyai University, Cluj-Napoca, Romania. [6]Université de Lorraine, CNRS, Institut Jean Lamour, Nancy, France. [7]Instituto Nicolás Cabrera (INC), Universidad Autónoma de Madrid, Madrid, Spain. [8]Condensed Matter Physics Institute (IFIMAC), Universidad Autónoma de Madrid, Madrid, Spain. [9]These authors contributed equally: César González-Ruano, Chenghao Shen, Pablo Tuero. ✉e-mail: zigor@buffalo.edu; farkhad.aliev@uam.es

there have been no measurements of the enhanced shot noise in such structures.

Conventional superconductivity is a condensation of Cooper pairs, consisting of electrons with opposite spins. Such spin-singlet superconductivity competes with ferromagnetism, which tends to align the electron spins parallel. In superconductor/ferromagnet (S/F) junctions, this competition lowers the superconducting critical temperature T_C and strongly suppresses the proximity effect, such that the characteristic length (-few nm) for superconductivity leaking into F is orders of magnitude shorter than in the S/normal metal (N) junctions[17–21]. However, if Cooper pairs are transformed to have equal (parallel) spins, the resulting equal-spin-triplet superconductivity would have the ability to coexist as a long-range triplet (LRT) with ferromagnetism, to transfer dissipationless spin currents, desirable for superconducting spintronics, and even to support elusive Majorana states for fault-tolerant topological quantum computing[17,22].

Rather than seeking the desired spin-triplet superconductivity in a single material such as Sr_2RuO_4, until recently expected to be a prime candidate[23], there is a growing effort to realize proximity-induced spin-triplet superconductivity in suitable junctions[17–19,21,22]. For two decades, such an approach to achieve LRT was focused on using complex ferromagnetic multilayers, typically relying on noncollinear or spiral magnetization[21,24–26] or half-metals[27–30]. More recently, interfacial spin-orbit coupling (SOC) was considered as an alternative platform, where proximity-induced spin-triplet superconductivity could be supported even with a single conventional ferromagnet[17,31]. In our work, using shot noise spectroscopy in high-quality epitaxial junctions, the significance of this SOC is even more striking. In the normal state, SOC determines the transport properties, while in the superconducting state, we address the long-standing search for the proximity-induced Josephson effect[32], enabled by the additional SOC-supported spin-triplet superconducting region.

Results

Our choice of epitaxial V(100)/MgO/Fe(100) junctions appears surprising. The incompatible orbital symmetries in the electronic structure of V(100) and Fe(100), suggest that their junctions are nonconducting in the low-bias regime[33–35]. Early experiments on heteroepitaxial superconducting Fe/V/Fe junctions reveal the importance of the relevant orbital symmetries and how they can determine desirable spin-dependent transport properties[36].

At the Fermi level E_F, Δ_2 orbital symmetry of V is absent for Fe, which is characterized by Δ_1 symmetry, shown in Fig. 1a. Since MgO is an insulator filtering out Δ_2 and producing giant tunneling magnetoresistance (TMR) in Fe/MgO/Fe junctions[33–35,37,38], proximity-induced superconductivity from V across MgO into Fe seems even less likely. However, structural inversion asymmetry in our junctions leads to interfacial SOC, which accompanies the effective Δ_2 barrier in crystalline MgO due to its filtering effect. The SOC-induced spin-flip scattering mixes Δ_2 and Δ_1 symmetries and creates a mechanism for electron tunneling above T_C across the junction at low bias, shown in Fig. 1a. Our first-principles calculations (see Supplementary Information, Section I, SI-I) also confirm the presence of Rashba SOC at the V/MgO interfaces. Another low-bias contribution in these epitaxial

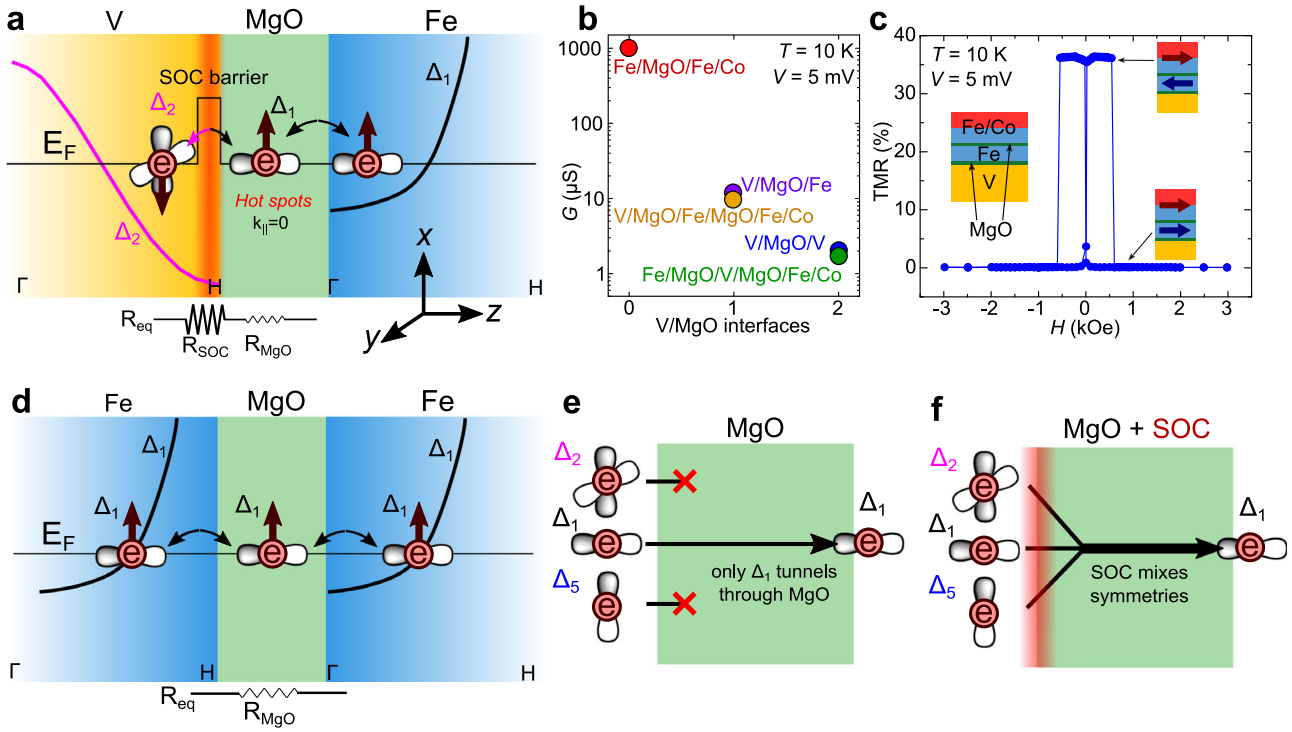

Fig. 1 | Orbital symmetry change and normal-state transport in epitaxial V/MgO/Fe-based junctions. a The main conductance bands, labeled with their respective orbital symmetries, are superimposed to each region. Arrows denote electron spin. At the Fermi level, E_F, in vanadium, only electrons with Δ_2 symmetry are present, while they are absent in iron. Therefore, a symmetry change is necessary for the electron transport across the V/MgO/Fe junction. This is enabled by the Rashba spin-orbit coupling (SOC) at the V/MgO interface. MgO acts both as (i) symmetry filter at E_F, relatively transparent for Δ_1 electrons in iron at the normal incidence (vanishing wave vector along the interface, $\mathbf{k}_{||} = 0$), while having a strong barrier for Δ_2 electrons and (ii) enabling the symmetry and spin changes allowing electron tunneling into the iron. An equivalent resistor model indicates that the SOC barrier dominates over the usual barrier from the MgO region. **b** Typical normal-state conductance of different tunnel junctions of a lateral size 20 × 20 μm^2, as a function of their number of V/MgO barriers. Each dot: sample-averaged conductance. Each extra V/MgO barrier diminishes the conductance by an order of magnitude. **c** In-plane tunnel magnetoresistance (TMR) of a spin-valve junction (inset), showing parallel and antiparallel magnetization configurations, changing with an applied magnetic field, H, and the typical coercive field of the hard Fe/Co magnetic layer. **d** Across the less-resistive Fe/MgO/Fe junction, the transport is dominated by Δ_1 electrons without SOC barrier. **e**, **f** The absence (presence) of SOC removes (enables) orbital symmetry mixing, explaining the measured relative magnitudes of conductance in (**b**).

https://doi.org/10.1038/s41467-025-64493-w

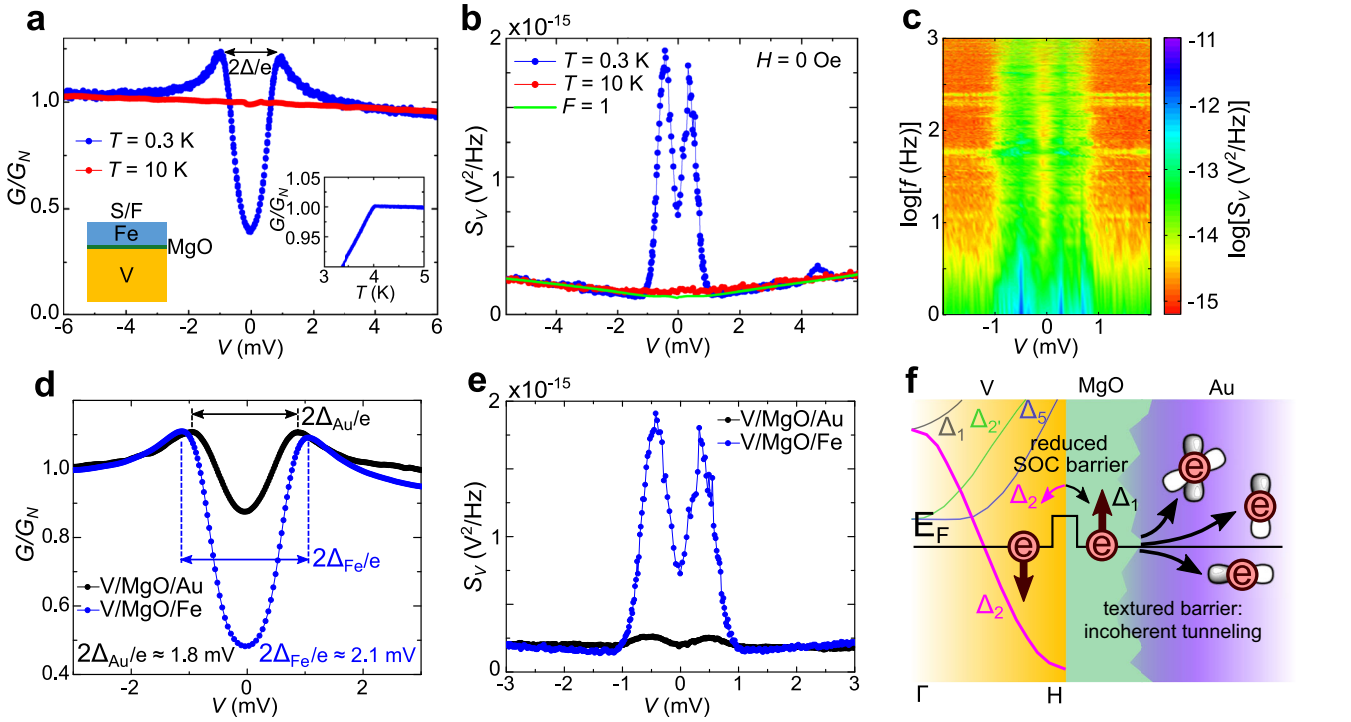

Fig. 2 | Bias dependence of the conductance and giant shot noise in a V/MgO/Fe junction. a Conductance for a superconductor/ferromagnet (S/F) sample (sketched in the left), above (red) and below (blue) the critical temperature of vanadium, T_C, normalized by the conductance at bias $V = -5$ mV, above the effective superconducting gap, Δ, -e is the electron charge. Inset: T_C identified by the measured temperature-dependent subgap conductance. **b** For the same sample, there is giant shot noise below T_C (blue) at low bias, $eV < \Delta$, compared to its value above T_C (red), and its corresponding theoretical maximum value given by the Fano factor, $F = 1$ (green), for the normal state. **c** The evolution of the shot noise power with frequency, f, and V, shown in the logarithmic scale. The noise spectrum is largely f independent, except near the lowest f. **d**, **e** Comparison of the bias-dependent conductance and shot noise with the control V/MgO/Au junction, with the same normalization as in (**a**). **f** Schematic role of the MgO/Au nonepitaxial growth leading to the highly textured interface and suppressed filtering due to different orbital symmetries.

junctions with conserved wave vector parallel to the interfaces, $\mathbf{k}_{||}$, comes from "hot spots" for normal incidence at $\mathbf{k}_{||} = 0$ (the Γ point), which provides high transmission through MgO[33]. A simple picture for the normal-state transport in this junction is described by an equivalent resistance, $R_{eq} = R_{SOC} + R_{MgO}$, in which the resistance of the symmetry-related SOC barrier, R_{SOC}, is much larger than the resistance from the conventional barrier strength of the MgO region, R_{MgO}.

This picture of the tunneling dominated by symmetry-enforced spin filtering, rather than by the barrier strength, is confirmed by the measured low-bias differential conductance G shown in Fig. 1b, revealing the key role of SOC at the V/MgO interface. Compared to junctions without such an interface, G is reduced by two (three) orders of magnitude with one (two) interface(s). For in-plane magnetization in a V/MgO/Fe/MgO/Fe/Co junction, shown in Fig. 1c, the obtained $TMR = (G_P - G_{AP})/G_{AP}$~40%, where G_P (G_{AP}) corresponds to parallel (antiparallel) magnetization in the two Fe regions, signals highly spin-polarized electrons. By excluding the nonmagnetic V/MgO region, we have shown an even higher TMR~330% in Fe/MgO/Fe/Co junctions[38]. Using shot noise measurements, we can also exclude the role of pinholes in determining G (details of sample fabrication, measurements, and characterization can be found in Methods, SI-II and Ref. 31). To further support our conductance measurements across different junctions, it is helpful to consider a schematic illustration of the role of dominant orbital symmetries and their SOC-induced mixing in Fig. 1d–f. The highest measured conductance in Fig. 1b is found for the Fe/MgO/Fe-based junction in which the dominant Δ_1 symmetry is shared by all the regions and the related transport does not experience the symmetry mismatch (no SOC barrier). However, for junctions with regions characterized by other orbital symmetries, the spin-filtering exclusion from the MgO can be overcome by SOC mixing and accompanied by a large R_{SOC}, consistent with the results in Fig. 1b.

In the superconducting state, as shown in Fig. 2a, transport is distinguished by Andreev reflection, providing the microscopic mechanism for proximity-induced superconductivity[13,17]. In conventional Andreev reflection, an electron is reflected backwards and converted into a hole of opposite charge and spin. With no interfacial barrier, this implies the doubling of the normal-state G_N: two electrons are transferred across the interface into S, where they form a spin-singlet Cooper pair[39]. Because of spin polarization P in F, not all electrons can find a partner of opposite spin to undergo Andreev reflection[17,40]. Together with the normal (ordinary) reflection at the interfacial barrier, such a finite P suppresses the Andreev reflection and reduces G[40] at applied bias $V < \Delta/e$ below the effective superconducting gap Δ ~1.05 meV, where -e is the electron charge. A small peak in $G(V \sim \Delta/e)$ and a substantial value of $G(V = 0)$ (Fig. 2a) suggest that S/F is not a typical tunnel junction and has only a moderate interfacial barrier strength. The inset in Fig. 2a indicates T_C ~ 4 K, as identified by the measured temperature-dependent conductance.

A high-quality MgO barrier defines the location of the voltage drop and thus enables accurate shot noise measurements, previously absent in S/F junctions. Unlike the measured $G(V)$, similar to what was observed in various superconducting structures, the shot noise in Fig. 2b for the same S/F junction shows an unprecedented giant low-bias increase at $T = 0.3\,\mathrm{K} < T_C$, orders of magnitude larger than theoretically expected. With fluctuations due to the discreteness of the electrical charge, it is common to introduce the current shot noise power $S_{I,max} = 2q\langle I\rangle$ transferred in discrete units of charge q, where $\langle I\rangle$ is the average current[10,11,41,42]. To describe the ratio between the shot noise and the conductance, it is useful to introduce the Fano factor[10,11] $F = S_I/(2eG|V|)$. This Fano factor also gives the effective charge responsible for the shot noise[10,11]. For a fully random (Poisson) process of uncorrelated electrons, $S_{Poisson} = 2e\langle I\rangle$, F in the normal

https://doi.org/10.1038/s41467-025-64493-w

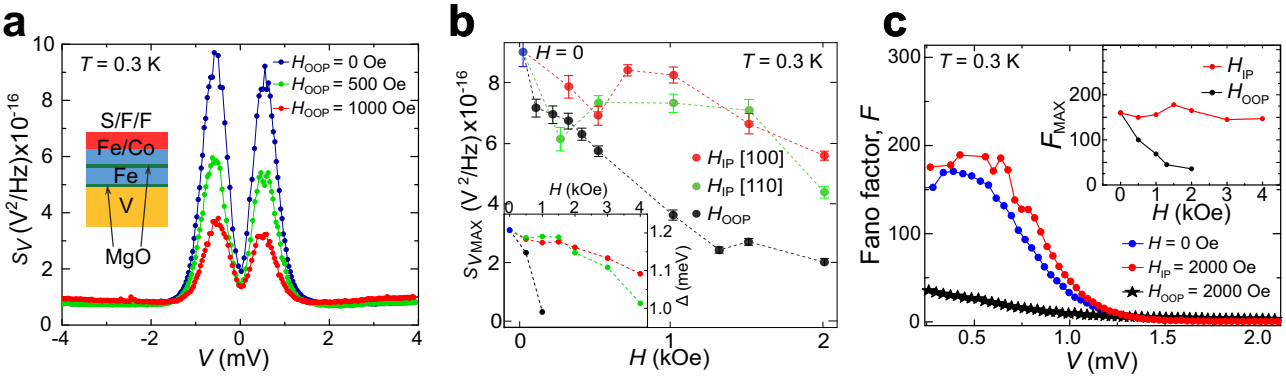

Fig. 3 | Anisotropic suppression of the giant shot noise by an applied magnetic field and bias. The measured spin-valve junction V/MgO/Fe/MgO/Fe/Co is the same as in Fig. 1c. **a** Out-of-plane (OOP) magnetic field effectively suppress the superconductivity and the observed low-bias shot noise. **b** Magnetic-field dependence of the maximum noise shot shows anisotropy, not only between in-plane (IP) and OOP (black), but also for IP easy (red) and hard (green) axis, which is unexpected for a spin-singlet superconductivity. Inset: anisotropic suppression of Δ for the same directions of applied magnetic field, H (same legend). **c** Evolution of the Fano factor, F, with applied bias and magnetic fields. The inset: the maximum Fano factor, F_{MAX}, shown for a wide range of IP (red) and OOP (black) applied fields.

state attains at maximum $F = 1$, while $F = 2$ for superconducting tunnel junctions[11] signals that $|q| = 2e$ since the shot noise originates from the transfer of Cooper pairs. With a finite circuit resistance, our measurements also include voltage fluctuations with the resulting voltage shot noise power[10,42,43] $S_V = F2e < I > /G^2$ (SI-II provides the expression for $T > 0$), shown together with the expected maximum normal-state value for $F = 1$. Remarkably, at $T = 0.3$ K and $eV < \Delta$, we can infer $F > 100$, as if a giant effective charge $|q| > 100$ e is responsible for the observed shot noise! This striking behavior is the hallmark of the superconducting state, while at $eV > \Delta$ or $T > T_C$, S_V approaches the Poisson value for $F = 1$ (green line). Another distinguishing feature of the giant S_V in the superconducting state is its independence of frequency f, shown in Fig. 2c over two orders of magnitude in the frequency range. In contrast, the contribution of vortices[43] is reflected in the $1/f$-dependent part of the noise, decreasing with f and increasing with T, when T approaches T_C (SI-III).

It is helpful to compare our prior conductance and shot noise results for S/I/F (V/MgO/Fe) junction with the measurements on a control S/I/N junction (V/MgO/Au). As expected, in Fig. 2d we find that the low-bias conductance is suppressed less in V/MgO/Au than that in V/MgO/Fe junction, consistent with the nonmagnetic Au and $P = 0$, as the Andreev reflection does not experience a large suppression from $P = 0.7$ at the Fe/MgO interface. Both junctions are not in a typical tunneling regime and they share only a small peak in G, known to appear at $V \sim \Delta/e$. However, the separation of the two peaks is larger in V/MgO/Fe where, considering the commonly expected competition between ferromagnetism and superconductivity[17,21], such a separation and the related superconducting gap should be reduced compared to the one in nonmagnetic V/MgO/Au. Since in both junctions we see that the superconducting gap exceeds the values expected for V itself, a larger peak separation in V/MgO/Fe would be consistent with a slightly larger proximity-induced gap than in V/MgO/Au (see discussion below). While the changes in the two corresponding gaps are moderate, turning to the comparison of the shot noise in Fig. 2e, we see a drastic increase in the measured low-bias shot noise of the V/MgO/Fe junction. These trends in the conductance and shot noise by replacing F by N region can be partially understood by recognizing the importance of the epitaxial growth and high-quality interfaces in V/MgO/Fe, while V/MgO/Au is an example of non-epitaxial growth leading to a highly textured interface and suppressed filtering due to different orbital symmetries, as depicted in Fig. 2f and SI-II. That the apparent superconducting gap is not more suppressed in V/MgO/Fe could signal the presence of spin-triplet superconductivity coexisting with ferromagnetism[17,31].

The correlations among electrons, due to Coulomb repulsion and the Pauli exclusion principle, reduce the shot noise below its Poisson limit $F = 1$ ($F = 2$) in the normal (superconducting) state[10,11]. For example, in the fractional quantum Hall effect, the measured $F = 1/3$ signals the characteristic fractional charge[4]. Rare exceptions where the shot noise is enhanced compared to the Poisson value[14–16] are typically observed in junctions with multiple superconducting regions without ferromagnets. To examine such excess shot noise, we consider a V/MgO/Fe/MgO/Fe/Co junction, used also to measure TMR in Fig. 1c. With the two different F regions, we can control the orientation of the Fe magnetization while the higher-coercivity Fe/Co magnetization remains fixed and serves as a sensor of the Fe magnetization through the measured *TMR* signal.

For the V/MgO/Fe/MgO/Fe/Co junction in Fig. 3a we see another example of a giant increase in the subgap shot noise, strongly suppressed by the out-of-plane (OOP) applied magnetic field, H_{OOP}. This is further examined in Fig. 3b, which shows the suppression of the maximum value of the subgap shot noise with both H_{OOP} and in-plane (IP) H_{IP}. A stronger S_V suppression with H_{OOP} than with H_{IP} is expected, just as for the OOP H-suppression of Δ (in the inset). However, the in-plane anisotropy (between [100] and [110] orientations for both S_V and Δ) is surprising for conventional spin-singlet superconductivity and could instead signal an induced spin-triplet superconductivity. We also observe a slight increase in the noise with H_{IP}, which can be attributed to the field-suppression of inherent magnetic textures. Similar trends in the suppression with V and H are also reproduced in the measured Fano factor in Fig. 3c, which reaches nearly $F = 200$.

To seek a possible explanation of this peculiar behavior, we recall that normal-state transport in V/MgO/Fe-based junctions and our first-principles calculations confirm the presence of the interfacial SOC. Given the measured H_{IP} noise anisotropy, such SOC influences the superconducting state and leads to spin-flip Andreev reflection with equal spin for electrons and holes, which is responsible for spin-triplet Cooper pairs[17,44,45]. As a result, SOC can partially counteract the suppression of Andreev reflection due to the high spin polarization, $P \sim 0.7$–0.8, of the Fe/MgO contact[31], and the normalized interfacial barrier strength Z, such that the resulting low-bias G is higher than without SOC[45]. This is consistent with the data from Fig. 2a, which indicate only a moderate $Z \sim 1$ ($Z = 0$ for perfect transparency and $Z \gg 1$ for a tunnel junction). However, when we theoretically explore the shot noise in S/F junctions over a large parameter space for normalized barrier and Rashba SOC strength Z and λ (see Methods and SI-IVA, B), respectively, the maximum value

https://doi.org/10.1038/s41467-025-64493-w

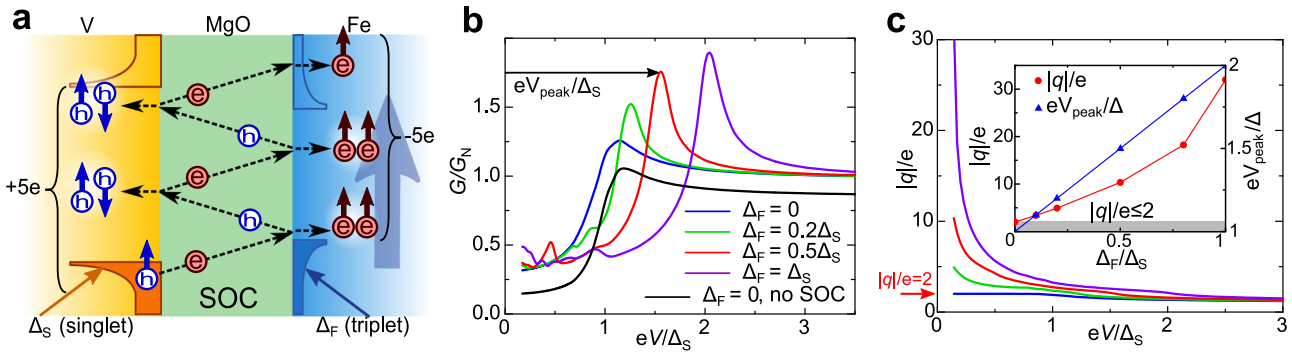

Fig. 4 | Physical mechanism with calculated conductance and shot noise. **a** Proximity-induced superconducting spin-triplet gap in Fe layer (blue), Δ_F, and the interfacial spin-orbit coupling (SOC) support multiple spin-flip Andreev reflections in the V/MgO/Fe junction, which give rise to the excess charge transport (5e in the sketch) and the resulting low-bias excess Fano factor, h denotes holes. **b** Bias-dependent conductance without (black) and with SOC (colored lines) for different relative magnitudes of the induced spin-triplet gap, Δ_F, and the spin-singlet gap, Δ_S, in vanadium. Without SOC, there is a reduced junction transparency and conductance for all V. For comparison with experimental measurements, each curve with SOC is normalized by its conductance value well above the superconducting gap. The barrier and SOC strengths are parameterized by $Z = 1$ and $\lambda = 1.2$ (see Methods). **c** Calculated Fano factor or, equivalently, the effective charge ratio $|q|/e$, as a function of applied bias for the same parameters and a color code as given in (**b**). Inset: The corresponding evolution of the effective charge ratio (at $eV/\Delta_S = 0.1$) and the conductance peak position with relative increase in Δ_F. The gray area denotes the commonly expected Fano factor limited by 2.

is $F = 2$ (SI-IVC), orders of magnitude smaller than in Figs. 2b or 3c. With our analysis of the calculated shot noise in an effective 1D system, in the absence of spin polarization, it is possible to analytically express different scattering coefficients for the S/N junction and use them to evaluate the enhanced Fano factor for S/N/S Josephson junctions (SI-IVD).

The interplay of ferromagnetism and SOC is expected to generate proximity-induced spin-triplet superconductivity, but that alone cannot explain a huge excess of shot noise. Instead, prior examples of large shot noise[14–16] suggest a resonant behavior which could naturally occur in Josephson junctions, with two superconducting regions and the formation of Andreev bound states, defined by multiple Andreev reflections (MAR)[20,46]. In the simple case of two identical superconducting gaps and $Z = 0$, one expects $n = \Delta/eV$ Andreev reflections, as if the charge transfer and the underlying shot noise could be described by a composite object with effective charge $|q| = ne$[47]. Support that only a single S region in nonmagnetic junctions could display properties of proximity-induced Josephson effect[32,47,48] motivates us to revisit the understanding of S/F junctions. Proximity-induced spin-singlet superconductivity is strongly suppressed in F, such as Fe. However, its SOC-induced spin-triplet counterpart could coexist with ferromagnets, and we also consider that it is accompanied by an effective superconducting gap Δ_F, and therefore supports MAR and enhances F beyond 2. The equal-spin superconducting correlations derived from the superconducting condensate inside V evolve dynamically through the interplay between SOC, symmetry-dependent tunneling, and the exchange interaction. The resulting phase evolution effectively decouples the proximity-induced superconducting correlations from the parent superconductor and supports MAR, which is also observed from preformed pairs[6,7]. This is unlike the usual proximity effects in S/F (S/N) junctions, where the proximitized order parameter is directly phase locked to that of S[21].

A sketch of the physical mechanism for the giant shot noise and induced Δ_F is depicted in Fig. 4a. The considered multiple electron-hole reflections are consistent with the abundance of these quasiparticles with Δ_1 symmetry at the Fermi level of Fe(001), which easily tunnel through the MgO due to hot spots in momentum space. Multiple states with complex wave vectors in the MgO lead to interference effects in G[31]. The Fano factor gives the effective charge transfer through MAR across the apparent proximity-induced Josephson junction, formed by the vanadium s-wave superconductor and the resulting spin-triplet correlations in Fe. With this picture, we generalize the MAR[15] calculation for G and the Fano factor to include the influence of SOC and normal reflections.

This simple phenomenological model, nevertheless, captures several important experimental observations. With the calculated G in Fig. 4b we see that SOC enhances the interfacial transparency, consistent with the measurements from Fig. 2a which indicate only a moderate $Z \sim 1$, rather than the conventional tunnel junction with $Z \gg 1$. By explicitly including $\Delta_F > 0$, we find that MAR-modified G no longer has the usual peak at the pure superconducting gap for vanadium, Δ_S, but is shifted to higher values, $eV_{peak} = \Delta_S + \Delta_F$. Considering the broadening effect on the G–V curve due to thermal smearing and inelastic scattering in experiments, this peak position could be further shifted to higher energies[49–51], leading to superconducting gaps (Δ_{Fe}, Δ_{Au}) in Fig. 2d that exceed the expected BCS value of $\Delta_S = 0.7$ meV for vanadium with a measured critical temperature of $T_C \sim 4$ K. Assuming that the spin-triplet gap is negligible in the S/I/N (V/MgO/Au) control junction and, based on the measured gaps (Δ_{Fe}, Δ_{Au}) in Fig. 2d, we find $\Delta_{Fe} / \Delta_{Au} = (\Delta_F + \Delta_S) / \Delta_S \approx 1.2$, from which we estimate the induced gap $\Delta_F \approx 20\%\ \Delta_S$. With these parameters, we achieve an excellent fit to the experimental conductance (Fig. 2a, SI-IVF). This peak shift effect provides additional evidence for the proximity-induced triplet gap and the Josephson junction-like behavior in the S/I/F (V/MgO/Fe) junction.

Considering next the Fano factor, which in Fig. 4c is represented by $|q|$, the calculated effective charge transfer (SI-IVE), we confirm the essential role of proximity-induced Δ_F, while a two-fold change of Z has only a very small influence. A finite Δ_F, through MAR, allows for a large number of electron pairs to be transferred into the superconducting lead, resulting in a giant F near vanishing V. In the opposite large-bias limit, $eV > \Delta$, $|q|$ approaches the uncorrelated limit e, as the current is carried by independent quasiparticles. However, with $\Delta_F = 0$, the higher-order Andreev reflections alternate between the electron and hole pairs transferred into the superconducting lead, without any giant Fano factor. Even at vanishing V, the calculated $|q|$ retains its conventional value of 2, known for S/N junctions[10]. The inset of Fig. 4c shows that the magnitude of the low-bias Fano factor grows with the increasing proximity-induced Δ_F, together with an increased bias value for the peak position in G. Even in the extreme limit of $\Delta_F = \Delta_S$, our calculated results underestimate the measured Fano factor. We attribute this limitation to our simple and transparent description, which neglects the random scattering from the SOC barrier and the destructive interference[52] suppressing the current (and therefore increasing F). Including these omitted effects could provide closer agreement with the measured Fano factor. Nevertheless, our

theoretical framework already addresses the observed major puzzle. We provide a mechanism to exceed the expected theoretical limit $F = 2$ (shown in gray) with a single S region, while using the same parameters that describe the measured $G(V)$ from Fig. 2a.

The significance of SOC and orbital symmetry selection in high-quality epitaxial junctions is further verified from our control V/MgO/V measurements (SI-II). One may expect that this conventional S/I/S Josephson junction would support an even larger Fano factor than in S/I/F junctions that we have studied. Indeed, experiments in NbN/MgO/NbN junctions confirm MAR and an enhanced shot noise[15]. Instead, with different orbital symmetries in V/MgO/V junctions, Δ_2 in vanadium and Δ_1 in MgO, both the conductance and subgap shot noise are suppressed several orders of magnitude as compared to V/MgO/Fe junctions.

These results suggest several important future opportunities. The proximity-induced Josephson effect in N/I/S junctions[47,48] was observed through I-V curves or a zero-bias conductance peak (ZBCP), reproducing properties of conventional S/I/S Josephson junctions. Since the origin of similar ZBCP observations[53] continues to be studied and attributed to resonant effects[54–56], even without the proximity-induced second superconducting region, our noise spectroscopy could distinguish various scenarios and detect the proximity-induced Josephson effect. Our focus on a simple and transparent theoretical approach invites future theoretical extensions. Resonant effects alone would not support MAR and preclude our observed giant shot noise. Another ZBCP implication is its signature of Majorana states[55] in spin-triplet topological superconductivity considered for fault-tolerant quantum computing[17,22]. However, an extrinsic ZBCP origin remains debated[22,57], and shot noise spectroscopy could help to identify Majorana states[58].

While Fe/MgO-based junctions have been extensively studied[34,35], from commercial applications[59] to integrating spintronics, electronics, and photonics[60], there is only a limited understanding of their all-epitaxial growth with superconductors[17,31]. Since we show that even in the normal state for these junctions, their resistance is dominated by the symmetry-related SOC barrier (recall Fig. 1b), rather than the conventional barrier associated with the MgO regions, this motivates further studies to explore the superconducting spintronics in all-epitaxial superconductor junctions with ferromagnets, where the spin-triplet proximity and spin currents could be controlled by SOC. The role of SOC in proximity-induced spin-triplet topological superconductivity is well studied using semiconductor nanostructures[17,22], but often overlooked in ferromagnetic junctions[21,28–30]. Shot noise spectroscopy could overcome these uncertainties, elucidating the role of SOC in systems where there remains a debate about the induced long-range spin-triplet superconductivity[30,61,62]. Our findings also pertain to materials design and emergent phenomena through various proximity effects, where buried interfaces play a crucial role[13]. While probing such interfacial properties poses a challenge for many scanning probes, our work demonstrates that even buried interfaces are directly accessible to noise spectroscopy.

Methods

Sample preparation and characterization

The magnetic tunnel junction (MTJ) multilayer stacks were grown by molecular beam epitaxy (MBE) in a chamber with a base pressure of $5{\cdot}10^{-11}$ mbar following the procedure described in Ref. 63. The samples were grown on (100) MgO substrates with a 10 nm thick seed of anti-diffusion MgO underlayer on the substrate to trap the C from it before the deposition of the Fe or V electrodes. Then the MgO insulating layer was epitaxially grown by e-beam evaporation with a thickness of approximately 2 nm and followed by the rest of the layers. Each layer was annealed at 450 °C for 20 mins for flattening. After the MBE growth, all the MTJ multilayer stacks were patterned in square junctions of a size from 10 to 40 μm (with the diagonal along [100]) by UV lithography and Ar ion etching, controlled step-by-step in situ by Auger spectroscopy. For the considered samples, the measured properties did not depend on the lateral size of our junctions.

For S/F junctions studied in the main text, the layer structure was V(40 nm)/MgO(2 nm)/Fe(10 nm). For S/F/F junctions, the base part V/MgO/Fe was the same, with an extra MgO(2 nm) barrier and a Fe(10 nm)/Co(20 nm) hard ferromagnetic layer grown on the top. The F/S/F junction structure was Fe(45 nm)/V(40 nm)/MgO(2 nm)/Fe(10 nm)/Co(20 nm), and the control S/S junctions had two 40 nm vanadium layers separated by a 2 nm thick MgO barrier.

Experimental measurement methods

The measurements were performed inside a JANIS® ^{3}He cryostat with a base temperature of 0.3 K. The magnetic field was varied using a 3D vector magnet consisting of one solenoid (Z axis) with $H_{max} = 3.5$ T and two Helmholtz coils (X and Y axis) with $H_{max} = 1$ T. In our system, the different magnetic states can be distinguished by looking at the resistance of these S/F/F junctions, so the relative orientation between the two F electrodes can be measured. The magnetoresistance measurements were performed by first setting the magnetic field to the desired value, then applying a positive and negative current up to the desired voltage (5 mV unless otherwise stated), and averaging the absolute values of the measured voltage for the positive and negative current, obtaining a mean voltage which was used to calculate the resistance at that point.

The electron current was supplied by a Keithley 220 low-noise current source. The voltage signal (DC + fluctuations) produced through the samples by this current was duplicated and then amplified, first by a homemade preamplifier (based on two INA111 instrumentation amplifiers), and then both channels were amplified again with two Stanford Research SR560 commercial amplifiers with the same configuration, which also filter out the DC component of the signal and apply a bandpass filter with a range that can be varied from 0 Hz to 1 MHz. For the differential conductance/resistance, the voltage was measured from one of the channels (which can be switched) with a Digital Multimeter PCI Board (DMM−552-PCI). Finally, both signals were sent to a Stanford Research SR785 spectrum analyzer which has a bandwidth of 102.4 kHz. The two inputs contain the sample noise signal δV_S and an extrinsic noise contribution δV_{amp} coming from the wires and the amplifiers. The noise from the sample is the same in both channels, but the extrinsic component due to the electronics of the voltage is uncorrelated between each channel, although of a similar magnitude. All the unnecessary electronic equipment was turned off to reduce external noise sources. The current was varied step by step and the voltage signal was duplicated and analyzed in the SRS785, performing cross-correlation to exclude the extrinsic part of the signal[42,64,65]. The cross-correlation technique allows us to decrease the background noise base level and to evaluate the frequency dependence of the noise power (see Fig. 1c in the main text) to exclude possible random telegraph noise contributions. To attain the same objective, other shot noise measurement systems with a single channel amplification only measure the noise within a narrow frequency band at higher frequencies[42].

Theoretical methods

To compute the transport noise, we extend a widely used approach for obtaining I-V characteristics and G[39,46] to decompose the electron distribution according to the number of Andreev reflections[15] in the Josephson current by keeping track of the net electron charge in each transmitted electron wavefunction. The effective charge in multiple Andreev reflections comes from coherent pair transport that greatly exceeds the charge of a pair of electrons. We first obtain scattering coefficients for the normal and Andreev reflection as well as the transmission in a single S/F junction with the SOC[44,45] from the

microscopic Bogoliubov-de Gennes Hamiltonian as a 4×4 matrix

$$\widehat{H} = \begin{pmatrix} \widehat{H}_e & \Delta_S \Theta(z) I_{2x2} \\ \Delta_S^* \Theta(z) I_{2x2} & \widehat{H}_h \end{pmatrix}, \tag{1}$$

$$\text{with } \widehat{H}_e = -\frac{\hbar^2}{2m^*}\nabla^2 - \mu - \frac{\Delta_{xc}}{2}\widehat{\mathbf{m}}\cdot\boldsymbol{\sigma}\Theta(-z) + \left[V_0 d + \alpha\left(k_y\sigma_x - k_x\sigma_y\right)\right]\delta(z) \tag{2}$$

and $\widehat{H}_h = -\sigma_y \widehat{H}^*_e \sigma_y$, where $\widehat{H}_e, \widehat{H}_h$ are the single-particle Hamiltonians for electrons and holes, while I_{2x2} is the two-dimensional unit matrix. Δ_S is the spin-singlet superconducting gap for vanadium, $\Theta(z)$ is the step function in the z direction, perpendicular to the S/F interface at $z = 0$, m^* is the effective electron mass, μ the chemical potential, Δ_{xc} the exchange spin splitting along the direction $\widehat{\mathbf{m}}$ of the magnetization. The interfacial scattering is modeled by a delta-function potential scattering, characterized by the effective barrier height V_0 and thickness d and the Rashba SOC strength α. $\sigma_{i=x,y,z}$ is the 2×2 Pauli matrix for the electron spin. It is convenient to introduce the dimensionless parameters for potential barrier and SOC strength[44,45]

$$Z = \frac{V_0 d m^*}{\hbar^2 k_F}, \lambda = \frac{2\alpha m^*}{\hbar^2} \tag{3}$$

In our calculations, we use $m^* = m_0$, where m_0 is the free-electron mass, and the chemical potential $\mu = 2.5$ eV. The spin polarization in the ferromagnet is $P = \Delta_{xc}/(2\mu) = 0.7$.

The scattering coefficients from the single junction are then used to compute the conductance and the effective charge $|q|$ in the F/S/F Josephson junction under bias by extending the approach[39,46], which neglects SOC and spin polarization. This formulation generalizes the electron distribution function[39] $f(E)$ at energy E decomposed as

$$f(E) = \sum_{N=0}^{\infty}\sum_{m=-\infty}^{\infty} g_m^N(E), \tag{4}$$

where the function $g_m^N(E)$ is resolved after N reflections from either of the S/F interfaces and m is the net electric current transmitted in the leads. Recursion relations for $g_m^N(E)$ after an additional reflection with the scattering coefficients from the S/F interfaces are derived in **SI-IVA,B**. The effective charge in the current noise is then computed with the transmission coefficient $T(E)$ as

$$\langle|q|\rangle = \frac{\sum_m |m| I_m}{\sum_m I_m} \text{ with } I_m = \sum_{N=0}^{\infty}\int T(E) g_m^N(E) dE. \tag{5}$$

A detailed formulation and more rigorous expressions are presented in **SI-IVA,B**, with an example demonstrated in a simple 1D limit in **SI-IVD**.

Data availability

The data supporting the findings of this study are available within the Article and its Supplementary Information files. This includes main trends in the theoretical results, given analytically in the Supplementary Information. The data for the calculations shown in Fig. 4 are available at the Figshare repository, under the following URL: https://doi.org/10.6084/m9.figshare.29988889. The raw data files for the experimental results are available from the corresponding authors upon request. Source data are provided with this paper.

Code availability

The computational code required to reproduce the theoretical calculations is available from the corresponding author upon reasonable request.

References

1. Harrow, A. W. & Montanaro, A. Quantum computational supremacy. *Nature* **549**, 203–209 (2017).
2. Kononchuk, R., Cai, J., Ellis, F., Thevamaran, R. & Kottos, T. Exceptional-point-based accelerometers with enhanced signal-to-noise ratio. *Nature* **607**, 697–702 (2022).
3. van der Weele, C. M. et al. Dopamine enhances signal-to-noise ratio in cortical-brainstem encoding of aversive stimuli. *Nature* **563**, 397–401 (2018).
4. Saminadayar, L., Glattli, D. C., Jin, Y. & Etienne, B. Observation of the e/3 fractionally charged Laughlin quasiparticle. *Phys. Rev. Lett.* **79**, 2526–2529 (1997).
5. Crooker, S. A., Rickel, D. G., Balatsky, A. V. & Smith, L. H. Spectroscopy of spontaneous spin noise as a probe of spin dynamics and magnetic resonance. *Nature* **431**, 49–52 (2004).
6. Bastiaans, K. M. et al. Direct evidence for Cooper pairing without a spectral gap in a disordered superconductor above Tc. *Science* **374**, 608–611 (2021).
7. Zhou, P. et al. Electron pairing in the pseudogap state revealed by shot noise in copper oxide junctions. *Nature* **572**, 493–496 (2019).
8. Weng, Q. C. et al. Imaging of nonlocal hot-electron energy dissipation via shot noise. *Science* **360**, 775–778 (2018).
9. Chen, L. et al. Shot noise in a strange metal. *Science* **382**, 907–911 (2023).
10. Blanter, Y.aM. & Buttiker, M. Shot noise in mesoscopic conductors. *Phys. Rep.* **336**, 1–166 (2000).
11. Beenakker, C. & Schonenberger, C. Quantum shot noise. *Phys. Today* **56**, 37–42 (2003).
12. Holm, R. & Meissner, W. Messungen mit hilfe von flüssigem Helium. XIII: Kontaktwiderstand zwischen supraleitern und nichtsupraleitern. *Z. Phys.* **74**, 715–735 (1932).
13. Žutić, I., Matos-Abiague, A., Scharf, B., Dery, H. & Belashchenko, K. Proximitized materials. *Mater. Today* **22**, 85–107 (2019).
14. Ronen, Y. et al. Charge of a quasiparticle in a superconductor. *Proc. Natl. Acad. Sci. USA* **113**, 1743–1748 (2016).
15. Dieleman, P., Bukkems, H. G., Klapwijk, T. M., Schicke, M. & Gundlach, K. H. Observation of Andreev reflection enhanced shot noise. *Phys. Rev. Lett.* **79**, 3486–3489 (1997).
16. Hoss, T. et al. Multiple Andreev reflection and giant excess noise in diffusive superconductor/normal-metal/superconductor junctions. *Phys. Rev. B* **62**, 4079–4085 (2000).
17. Amundsen, M., Linder, J. & Robinson, J. W. A. Žutić, I. & Banerjee, N. Colloquium: Spin-orbit effects in superconducting hybrid structures. *Rev. Mod. Phys.* **96**, 021003 (2024).
18. Eschrig, M. Spin-polarized supercurrents for spintronics: A review of current progress. *Rep. Prog. Phys.* **78**, 104501 (2015).
19. Linder, J. & Robinson, J. W. A. Superconducting spintronics. *Nat. Phys.* **11**, 307–315 (2015).
20. Tafuri, F. ed. Fundamentals and Frontiers of the Josephson Effect (Springer Nature, Cham, 2019).
21. Buzdin, A. I. Proximity effects in superconductor-ferromagnet heterostructures. *Rev. Mod. Phys.* **77**, 935–976 (2005).
22. Flensberg, K., Von Oppen, F. & Stern, A. Engineered platforms for topological superconductivity and Majorana zero modes. *Nat. Rev. Mater.* **6**, 944–958 (2021).
23. Abergel, D. Triplet no more. *Nat. Phys.* **15**, 1105–1106 (2019).
24. Bergeret, F. S., Volkov, A. F. & Efetov, K. B. Odd triplet superconductivity and related phenomena in superconductor-ferromagnet structures. *Rev. Mod. Phys.* **77**, 1321–1373 (2005).
25. Robinson, J. W. A., Witt, J. D. S. & Blamire, M. G. Controlled injection of spin-triplet supercurrents into a strong ferromagnet. *Science* **329**, 59–61 (2010).
26. Diesch, S. et al. Creation of equal-spin triplet superconductivity at the Al/EuS interface. *Nat. Commun.* **9**, 5248 (2018).

27. Eschrig, M., Kopu, J., Cuevas, J. C. & Schon, G. Theory of half-metal/superconductor heterostructures. *Phys. Rev. Lett.* **90**, 137003 (2003).
28. Keizer, R. S. et al. A spin triplet supercurrent through the half-metallic ferromagnet CrO2. *Nature* **439**, 825–827 (2006).
29. Singh, A., Voltan, S., Lahabi, K. & Aarts, J. Colossal proximity effect in a superconducting triplet spin valve based on the half-metallic ferromagnet CrO2. *Phys. Rev. X* **5**, 021019 (2015).
30. Sanchez-Manzano, D. et al. Extremely long- range, high-temperature Josephson coupling across a half-metallic ferromagnet. *Nat. Mater.* **21**, 188–194 (2022).
31. Martínez, I. et al. Interfacial spin-orbit coupling: A platform for superconducting spintronics. *Phys. Rev. Appl.* **13**, 014030 (2020).
32. Ferrell, R. A. Fluctuations and the superconducting phase transition: II. Onset of Josephson tunneling and paraconductivity of a junction. *J. Low. Temp. Phys.* **1**, 423–442 (1969).
33. Butler, W. H., Zhang, X.-G., Schulthess, T. C. & MacLaren, J. M. Spin-dependent tunneling conductance of Fe/MgO/Fe sandwiches. *Phys. Rev. B* **63**, 054416 (2001).
34. Parkin, S. S. P. et al. Giant tunneling magnetoresistance at room temperature with MgO (100) tunnel barriers. *Nat. Mater.* **3**, 862–867 (2004).
35. Yuasa, S., Nagahama, T., Fukushima, A., Suzuki, Y. & Ando, K. Giant room temperature magneto-resistance in single-crystal Fe/MgO/Fe magnetic tunnel junctions. *Nat. Mater.* **3**, 868–871 (2004).
36. Miao, G.-X., Ramos, A. V. & Moodera, J. S. Infinite magnetoresistance from the spin dependent proximity effect in symmetry driven bcc–Fe/V/Fe heteroepitaxial superconducting spin valves. *Phys. Rev. Lett.* **101**, 137001 (2008).
37. Lu, Y. et al. Spin-orbit coupling effect by minority interface resonance states in single-crystal magnetic tunnel junctions. *Phys. Rev. B* **86**, 184420 (2012).
38. Guerrero, R., Herranz, D. & Aliev, F. G. High bias voltage effect on spin-dependent conductivity and shot noise in carbon-doped Fe(001)/MgO(001)/Fe(001) magnetic tunnel junctions. *Appl. Phys. Lett.* **91**, 132504 (2007).
39. Blonder, G. E., Tinkham, M. & Klapwijk, T. M. Transition from metallic to tunneling regimes in superconducting microconstrictions: Excess current, charge imbalance, and supercurrent conversion. *Phys. Rev. B* **25**, 4515–4532 (1982).
40. Žutić, I. & Das Sarma, S. Spin-polarized transport and Andreev reflection in semi-conductor/ superconductor hybrid structures. *Phys. Rev. B* **60**, R16322–R16325 (1999).
41. Niu, J. et al. Why shot noise does not generally detect pairing in mesoscopic superconducting tunnel junctions. *Phys. Rev. Lett.* **132**, 076001 (2024).
42. Aliev F. G. & Cascales, J. P. Noise in Spintronics: From Understanding to Manipulation (Stanford Publishing, 2018).
43. Anton, S. M. et al. Magnetic flux noise in dc SQUIDs: Temperature and geometry dependence. *Phys. Rev. Lett.* **110**, 147002 (2013).
44. Högl, P., Matos-Abiague, A., Žutić, I. & Fabian, J. Magnetoanisotropic Andreev reflection in ferromagnet/superconductor junctions. *Phys. Rev. Lett.* **115**, 116601 (2015).
45. Vezin, T., Shen, C., Han, J. E. & Žutić, I. Enhanced spin-triplet pairing in magnetic junctions with s-wave superconductors. *Phys. Rev. B* **101**, 014515 (2020).
46. Octavio, M., Tinkham, M., Blonder, G. E. & Klapwijk, T. M. Subharmonic energy-gap structure in superconducting constrictions. *Phys. Rev. B* **27**, 6739–6746 (1983).
47. Han, S., Cohen, F. & Wolf, E. L. Apparent critical currents and rf steps in a second-order proximity-induced Josephson effect. *Phys. Rev. B* **42**, 8682–8685 (1990).
48. Agraït, N., Rodrigo, J. G. & Vieira, S. Transition from the tunneling regime to point contact and proximity-induced Josephson effect in lead-normal-metal nanojunctions. *Phys. Rev. B* **46**, 5814(R) –5817(R) (1992).
49. Nadgorny, B. E. Point Contact Andreev Reflection Spectroscopy, in Spintronics Handbook: Spin Transport and Magnetism, 2nd Ed., edited by Tsymbal, E. Y. & Žutić, I. (CRC Press, Boca Raton, FL, 2019), Vol. 3, pp. 35-97.
50. Sheet, G., Mukhopadhyay, S. & Raychaudhuri, P. Role of critical current on the point-contact Andreev reflection spectra between a normal metal and a superconductor. *Phys. Rev. B* **69**, 134507 (2004).
51. Shigeta, I. et al. Epitaxial contact Andreev reflection spectroscopy of NbN/Co2FeSi layered devices. *Appl. Phys. Lett.* **112**, 072402 (2018).
52. Lee, P. A. & Ramakrishnan, T. V. Disordered electronic systems. *Rev. Mod. Phys.* **57**, 287–337 (1985).
53. Kastalsky, A. et al. Observation of pair currents in superconductor-semiconductor contacts. *Phys. Rev. Lett.* **67**, 3026–3029 (1991).
54. Bouscher, S. et al. Enhanced Cooper-Pair Injection into a Semiconductor Structure by Resonant Tunneling. *Phys. Rev. Lett.* **128**, 127701 (2022).
55. Giazotto, F. et al. Resonant transport in Nb/GaAs/AlGaAs heterostructures: Realization of the de Gennes–Saint-James model. *Phys. Rev. Lett.* **87**, 216808 (2001).
56. Sengupta, K., Žutić, I., Kwon, H.-J., Yakovenko, V. M. & Das Sarma, S. Midgap edge states and pairing symmetry of a quasi-one-dimensional organic superconductor. *Phys. Rev. B* **63**, 144531 (2001).
57. Yu, P. et al. Non-Majorana states yield nearly quantized conductance in proximatized nanowires. *Nat. Phys.* **17**, 482–488 (2021).
58. Jonckheere, T. et al. Giant shot noise from Majorana zero modes in topological trijunctions. *Phys. Rev. Lett.* **122**, 097003 (2019).
59. Spintronics Handbook: Spin Transport and Magnetism, 2nd Ed., edited by Tsymbal, E. Y. & Žutić, I.(CRC Press, Boca Raton, FL, 2019).
60. Dainone, P. A. et al. Controlling the helicity of light by electrical magnetization switching. *Nature* **627**, 783–788 (2024).
61. Kalcheim, Y., Kizhner, T., Koren, G. & Millo, O. Long-range proximity effect in La2/3Ca1/3MnO3/ (100)YBa2Cu3O7–δ ferromagnet/superconductor bilayers: Evidence for induced triplet superconductivity in the ferromagnet. *Phys. Rev. B* **83**, 064510 (2011).
62. Fridman, I., Gunawan, L., Botton, G. A. & Wei, J. Y. T. Scanning tunneling spectroscopy study of c-axis proximity effect in epitaxial bilayer manganite/cuprate thin films. *Phys. Rev. B* **83**, 104522 (2011).
63. Tiusan, C. et al. Spin tunneling phenomena in single crystal magnetic tunnel junction systems. *J. Phys.: Condens. Matter* **19**, 165201 (2007).
64. Walls, W. F. Cross-correlation phase noise measurements, Proceedings of the 1992 IEEE Frequency Control Symposium, 257-261 (1992).
65. Cascales, J. P. Conductance and Noise in Magnetic Tunnel Junctions with inorganic and organic barriers, PhD Thesis, Universidad Autónoma de Madrid Requests for materials should be addressed to Farkhad Aliev or Igor Žutić (2015).

Acknowledgements

The work in Madrid was supported by the Spanish Ministry of Science and Innovation (PID2021-124585NB-C32, TED2021-130196B-C22, PID2024-155399NB-I00) (F.G.A.) and Consejería de Educación e Investigación de la Comunidad de Madrid (Mag4TIC-CM Ref. TEC-2024/TEC-38) (F.G.A.). grants. Financial support from the Spanish Ministry of Science and Innovation, through the María de Maeztu Program for Units of Excellence in R&D CEX2023-001316-M is also acknowledged (F.G.A.). The work in Buffalo was supported by the US Department of Energy (DOE) Office of Science Basic Energy Sciences (BES) award no. DE-SC0004890 (C.S., I.Ž.). Computational resources were provided by the UB Center for Computational Research. C. T. acknowledges the following funding sources: the project "MODESKY" ID PN-III-P4-ID-PCE-

2020-0230-P, grant No. UEFISCDI: PCE 245/02.11.2021 and the BBU grants AGC30199/17.01.2025, AGC30200/17.01.2025 and GS-UBB-FF - Coriolan Tiusan/2025 (C.T.). The support by the French National Research Agency (ANR) SOTspinLED project (no. ANR-22-CE24-0006-01), CHIFTS project (No. ANR-23-CE09-0006-003), and PEPR-SPIN OptoSpinCom project (No. ANR-24-EXSP-0010) is also acknowledged (Y.L.). The growth of samples was performed using equipment from the CC-DAUM platform funded by FEDER (EU), ANR, the Region Lorraine, and the metropole of Grand Nancy.

Author contributions

Y.L. and C.T. fabricated the samples and performed structural characterization. C.G.-R. and P.T. measured and analyzed the conductance and noise with the guidance of F.G.A. C.S., J.E.H., and I.Ž. contributed to theoretical understanding and modeling. C.T. carried out ab initio simulations. F.G.A. designed the overall experiment. F.G.A. and I.Ž. wrote the manuscript with the input and help of C.G-R., J.E.H., C.S., and C.T. All authors discussed the results and commented on the manuscript. C. G-R, P. T., and C. S. contributed equally to the manuscript.

Competing interests

The authors declare no competing interests.

Additional information

Supplementary information The online version contains supplementary material available at https://doi.org/10.1038/s41467-025-64493-w.

Correspondence and requests for materials should be addressed to Igor Žutić or Farkhad G. Aliev.

Peer review information *Nature Communications* thanks the anonymous reviewers for their contribution to the peer review of this work. A peer review file is available.